Buckling analysis of I-section portal frames with stochastic imperfections

Vissarion Papadopoulos *, George Soimiris, Manolis Papadrakakis

Institute of Structural Analysis and Seismic Research, National Technical University of Athens, Iroon Polytechniou 9, Zografou Campus, Athens 15780, Greece

ABSTRACT

This work examines the effect of random geometric imperfections in the buckling response of I-profile steel beam–column members as well as portal frame structures. Geometric imperfections are assumed to be non-homogeneous Gaussian random fields. Samples of these fields are generated using the spectral representation method with evolutionary power spectra derived from experimental measurements using the method of separation. A number of samples of random imperfect geometries are generated and simulated with detailed discretization with triangular shell finite elements. The stochastic buckling loads are determined in the context of brute force Monte Carlo simulation by repeated material and geometrically nonlinear finite element analyses. Single beam–column members are subjected to pure axial compression while the portal frames are tested for lateral loading. Various types of boundary conditions are implemented and histograms of bucking loads are derived for each case examined leading to useful conclusions for this type of structures, regarding imperfection triggered buckling response and buckling load variability.

1. Introduction

The wide usage of thin-walled slender members of steel structures has made necessary the study of their behavior under various types of loading and boundary conditions. These members are preferred because they lead to light-weighted and economic constructions and are proven to have a more efficient load-carrying behavior especially under bending. However, the structural response of a thin-walled I-section member is sensitive to imperfections that are created in the web and the flanges during the manufacturing process or during the transportation and the placement in the building site [1,2]. These imperfections are predominantly geometric imperfections referring to the deviation of the geometry from ideal shape of the member.

Various methods have been developed in order to simulate numerically initial imperfections. Conventional deterministic approaches assume that imperfections are in the form of critical eigenmodes of the perfect structure [3–5], while probabilistic approaches were mainly implemented by treating the Fourier coefficients obtained by series expansion of corresponding experimental measurements as random variables [6–9]. However, a realistic description of initial imperfections in a rational probabilistic framework is absolutely necessary in order to capture the discrepancy between observed and predicted buckling loads as well as the large scatter that these loads usually exhibit. Towards this aim, a

number of works was emerged in the last decade, treating the imperfections as stochastic fields which can be simulated with a standard numerical procedure such as Karhunen–Loeve expansion or the spectral representation method [10–19]. These stochastic approaches were mainly introduced for shell type structures, while a variant of these methods was recently applied for short-length I beam–column structural elements which exhibit a predominant local buckling behavior [20]. In that work, the "method of separation" was proposed for capturing the non-homogeneous characteristics of initial imperfections which proved very accurate, with optimum localization in space and frequency domain. Furthermore, the method proved efficient in deriving evolutionary power spectra (EPS) from samples of narrow banded separable stochastic fields, such as initial imperfections [20–22].

The present paper examines the effect of random geometric imperfections in I-profile beam–column steel members, with predominant global buckling modes, as well as steel portal frame structures. Geometric imperfections are assumed to be non-homogeneous Gaussian random fields. Samples of these fields are generated using the spectral representation method, having previously estimated the corresponding evolutionary power spectra (EPS) using the method of separation and real measurements of imperfections. A number of samples of random imperfect geometries are generated and simulated with detailed discretization with 3-noded triangular shell finite elements. The stochastic buckling loads are determined in the context of brute force Monte Carlo simulation by repeated material and geometrically nonlinear finite element analyses. Single beam–column members are subjected to

---

* Corresponding author. Tel.: +30 210 772 4158.
  E-mail address: vpapado@central.ntua.gr (V. Papadopoulos).

pure axial compression while the portal frames are tested for lateral loading. Various types of boundary conditions are implemented and histograms of bucking loads are derived for each case examined leading to useful conclusions for this type of structures, regarding imperfection triggered buckling response and the buckling load variability.

2. Stochastic finite element method (SFEM)

SFEM represents a combination of two important methodologies that are used for the solution of complicated problems of modern mechanics: the finite element method and stochastic analysis. The latter is based on reliability analysis, signal processing and probability theory [23–28]. In SFEM analysis random parameters are modeled as stochastic fields with statistical properties based on corresponding experimental measurements when available.

A one dimensional homogeneous zero-mean random field $f(x)$ can be easily described by its mean and autocorrelation function as follows:

$$\mu_f(x) = E[f(x)] \tag{1a}$$

$$R_{ff}(x_1, x_2) = E[f(x_1)f(x_2)] = R_{ff}(x_1, x_1 + \tau) = R_{ff}(\tau) \tag{1b}$$

where $E[\ ]$ denotes the mathematical expectation and $\tau = x_2 - x_1$.

Applying the Fourier transform on the autocorrelation function we obtain the power spectrum as:

$$S_{ff}(\omega) = \frac{1}{2\pi} \int_{-\infty}^{+\infty} R_{ff}(\tau) \exp(-i\omega x) d\tau \tag{2}$$

A non-zero stochastic field can be described as the sum of its deterministic mean function $\mu(x)$ and a zero-mean field $f(x)$, as follows:

$$h(x) = \mu(x) + f(x) \tag{3}$$

On the other hand, in non-homogeneous random fields the power spectrum depends not only on the frequency ω but also on the spatial state variable x. In cases in which these spectra are separable (or approximately separable) which, as demonstrated in [21], is definitely the case of initial imperfections of I-section steel members, the corresponding evolutionary power spectrum can be expressed as the product of a homogeneous power spectrum $S_h(\omega)$ and a spatial envelope function $g_h(x)$ as follows:

$$S(\omega, x) = S_h(\omega) \cdot g_h(x) \tag{4}$$

2.1. The method of separation

Various methodologies have been proposed in the past for estimating EPS from available experimental measurements, i.e. from real samples of stochastic signals. Among them the most widely used are the short-time Fourier transform and the wavelet-based EPS estimation [29–33]. The basic disadvantage of these approaches is that they cannot achieve simultaneous resolution in space and frequency domains. A novel methodology was proposed in [21] to obtain estimates of EPS in cases of separable processes. This method is based on simple principles of stochastic process theory and for this reason it is easy to implement and computationally efficient, while at the same time proved to be accurate with optimum simultaneous resolution in space and frequency [20–22].

According to this approach an estimate of the first term in Eq. (4) can be readily obtained by averaging the periodograms over the ensemble:

$$\bar{S}_h(\omega) = E\left[\frac{1}{2\pi L}\left|\int_0^L f^{(i)}(x) \cdot e^{-I\omega x} dx\right|^2\right] \tag{5}$$

while an estimate of the spatial envelope function can be obtained from the distribution of the mean square over the samples as follows:

$$\bar{g}_h(x) = \frac{E\left[|f^{(i)}(x)|^2\right]}{2\int_0^\infty \bar{S}_h(\omega)d\omega} \tag{6}$$

It can be easily shown that an unbiased estimate of the evolutionary power spectrum may be obtained as follows [21]:

$$\bar{S}_h(\omega, x) = E\left[|f^{(i)}(x)|^2\right]\frac{\bar{S}_h(\omega)}{2\int_0^\infty \bar{S}_h(\omega)d\omega} \tag{7}$$

2.2. Spectral representation

Having estimated the EPS from a series of experimentally measured imperfections, samples of imperfection field can be generated using the spectral representation method, as follows:

$$\hat{f}(x) = \sqrt{2}\sum_{n=0}^{N-1} A_n \cos(\omega_n x + \varphi_n) \tag{8}$$

where

$$A_n = \sqrt{2S(\omega_n, x)\Delta\omega}, n = 0, 1, \ldots, N-1$$
$$\omega_n = n\Delta\omega, n = 0, 1, \ldots, N-1$$
$$\Delta\omega = \frac{\omega_{up}}{N} \tag{9}$$
$$A_0 = 0, S(\omega_0, x) = 0$$

The parameter ω_{up} refers to an upper limit of the frequency, beyond which the power spectrum is supposed to be zero. Parameter φ_n expresses random phase angles and takes values in the field $[0, 2\pi]$ so that:
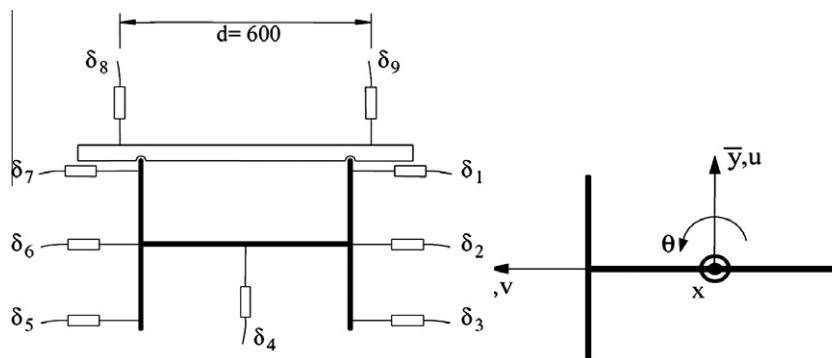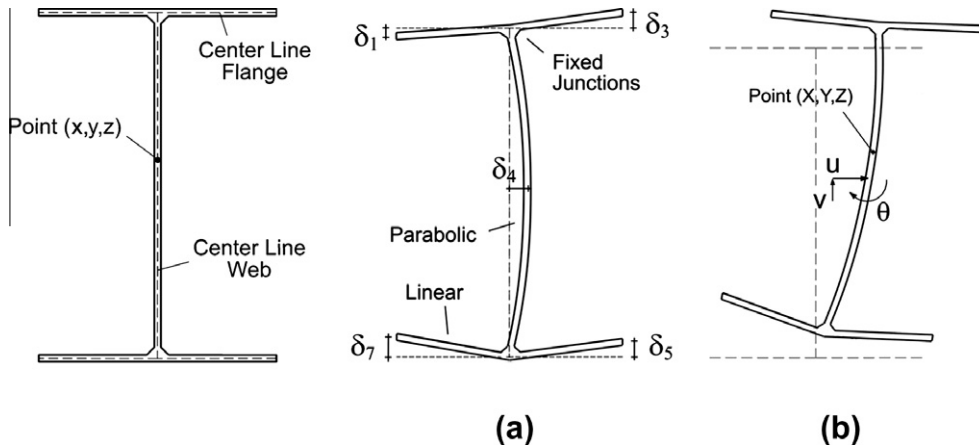

Fig. 1. Local and global imperfections.

Fig. 2. Mapping from perfect to imperfect geometry: (a) local and (b) global imperfection modes.

$$p(\varphi_n) = \begin{cases} 1/2\pi & 0 \leqslant \varphi_n 2\pi \\ 0 & else \end{cases} \qquad (10)$$

2.3. Monte Carlo simulations (MC)

Generally, the implementation of MC method consists of numerically simulating a population corresponding to the random quantities in the physical problem, solving the deterministic problem associated with each member of the population, and obtaining a population corresponding to the random response quantities, that can be used to obtain statistics of the response variables [34–36]. In the present study, the Monte Carlo simulation is implemented with a large number of FEM analyses, taking into account randomly generated samples of geometric imperfections, for the computation of the corresponding critical buckling loads. Furthermore, histograms are prepared by statistically processing the computed results, showing the distribution of the buckling loads for each case examined. In the present study, the stochastic analysis is referred only to the initial geometric imperfections while all other geometric and material properties of the members are assumed deterministic.

3. Modeling of random imperfections

Experimental measurements of imperfections were taken from Hasham and Rasmussen [37]. These data refer to a total of nine global and local imperfections of the cross-sections, as shown in Fig. 1 (δ_1–δ_9). These measurements have been performed on the free edges of the flanges (δ_1, δ_3, δ_5, δ_7), on the centre of the cross-section (δ_4), on web-flange junctions (δ_2, δ_6) and on the outer edges of the flanges (δ_8, δ_9). From δ_2, δ_6, δ_8 and δ_9, the three global imperfections which correspond to the two global translations u, v and the global rotation θ of the cross-section, are extracted with reference to Fig. 1 as follows:

$$u = \frac{(\delta_8 + \delta_9)}{2}, \quad v = \frac{(\delta_2 - \delta_6)}{2}, \quad \vartheta = \frac{(\delta_9 - \delta_8)}{600} \qquad (11)$$

The local imperfections are considered directly as the δ_1, δ_3, δ_4, δ_5 and δ_7 measurements.

Samples of the imperfect geometry are then constructed by the following mapping:

$$\begin{bmatrix} Y \\ Z \end{bmatrix}(x,y,z) = \begin{bmatrix} y \\ z \end{bmatrix} + \underbrace{\begin{bmatrix} \Delta Y_{glob} \\ \Delta Z_{glob} \end{bmatrix}(x,y,z)}_{global} + \underbrace{\begin{bmatrix} 0 \\ \Delta Z_{flg,i}(x)\frac{y_i}{w} \end{bmatrix} + \begin{bmatrix} \Delta Y_{web}(x)(1-\frac{z_i^2}{H}) \\ 0 \end{bmatrix}}_{local} \qquad (12)$$

where as shown in Fig. 2, (x, y, z) are the coordinates of the perfect geometry of the I profile section and (X, Y, Z) are the coordinates of the distorted section with $x = X$ and w is the flange length and H the web height. In the above equation, ΔY_{glob} and ΔZ_{glob} correspond to the global imperfection components given by [20]:

$$\begin{bmatrix} \Delta Y_{glob} \\ \Delta Z_{glob} \end{bmatrix}(x,y,z) = \begin{bmatrix} U \\ V \end{bmatrix}(x) + \begin{bmatrix} f_u \\ f_v \end{bmatrix}(x) + \begin{bmatrix} \cos(\Theta+f_\theta) & -\sin(\Theta+f_\theta) \\ \sin(\Theta+f_\theta) & \cos(\Theta+f_\theta) \end{bmatrix}(x) \cdot \begin{bmatrix} y \\ z \end{bmatrix} \qquad (13)$$

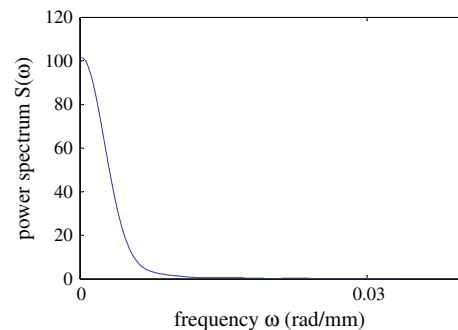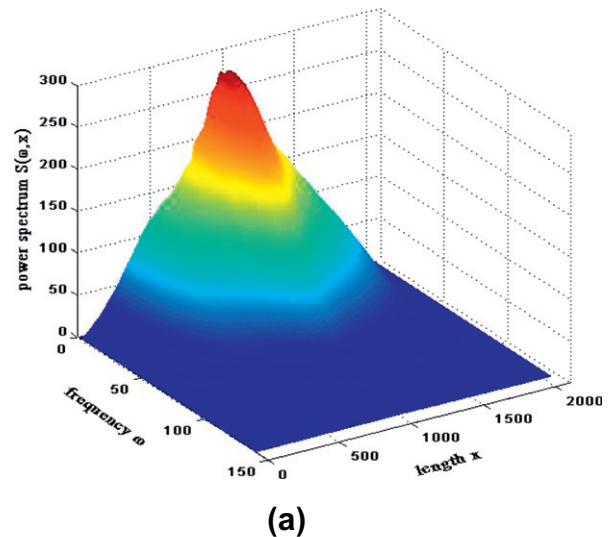**(a)**

(b)

Fig. 3. (a) EPS of global imperfection u and (b) homogeneous power spectrum of local imperfection δ_1.
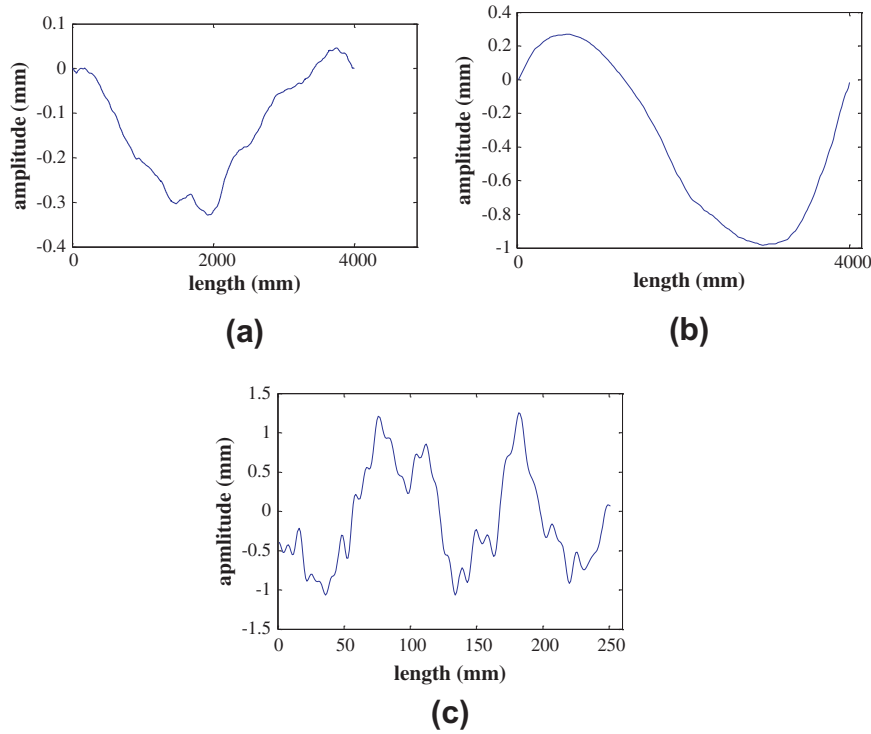
Fig. 4. (a) Mean value of global imperfection U, (b) one sample of global imperfection u, and (c) one sample of local imperfection δ_1.

In the above Eq. (13) the global components are extracted from the corresponding measurements u, v and θ (see Eq. (11)). The corresponding mean values of these measurements are denoted as $U(x)$, $V(x)$ and $\Theta(x)$ for the two translations and the rotation respectively, while $f_u(x), f_v(x)$ and $f_\theta(x)$ are zero mean evolutionary stochastic fields describing the fluctuations of the global imperfections around their mean values and for which the evolutionary power spectra are calculated with the method of separation. For the local components of Eq. (12), $\Delta Z_{flg,i}(x)$ is a stochastic field generated independently for each flange i, while $i = 1, 2, 3, 4$ corresponding to the experimental measurements δ_1, δ_3, δ_5 and δ_7, respectively. This field is assumed to be zero mean and homogeneous throughout its length. Similarly, $\Delta Y_{web}(x)$ is the stochastic field extracted from δ_4. A linear interpolation of flange imperfections is assumed for the outer flange edge until the web assuming zero imperfections at the flange connection to the web. A quadratic interpolation is assumed for the distribution of the web imperfections along the web height with zero value at the connections with the flanges and δ_4 at the central web point (see Fig. 2).

Fig. 3a presents the EPS computed for global u imperfection mode, while Fig. 3b presents the homogenous power spectrum of local zero mean imperfection mode δ_1. Fig. 4 depicts the calculated mean value $U(x)$, as well as randomly selected sample functions of δ_1 and u respectively. A sample realization of the complete imperfect geometry of the member generated using Eq. (12), is plotted in Fig. 5. All imperfections are scaled by a factor $\lambda = 15$ for visualization purposes.

4. Numerical examples

4.1. I-section beam–column members

A number of 4 m long beam–column members under compression are examined in this section. Three different boundary conditions were implemented. In the first case (case A) a fully fixed condition is assumed on both member's end-sections, i.e. all nodes restrained against translations and rotations, except at the end-section of the applied axial load, in which only the translations along the member axis are released. In the second case (case B) a fixed condition is again assumed for the one end-section but with the following difference with respect to case A: Rotations along cross-sectional major axis are released to allow rotations of the web and flanges, while the overall end-section rotation remains fixed. Fig. 6a and b present the deformed shapes of the end-sections for cases A and B, respectively. A partially fixed condition is assumed for the other end-section with the middle node of the section restrained against all rotations and translations except from the one along the member axis and the cross-sectional major axis rotation. According to the above, the beam–column member has its one end fixed and the other, where the loading is applied, pinned on the x–z plane, but both ends are fixed on the x–y plane. In the third case (case C) both end-sections are assumed partially fixed as described above, which means that they are both pinned on the x–z plane and fixed on the x–y plane. A schematic representation of the three boundary condition cases is presented in Fig. 7.
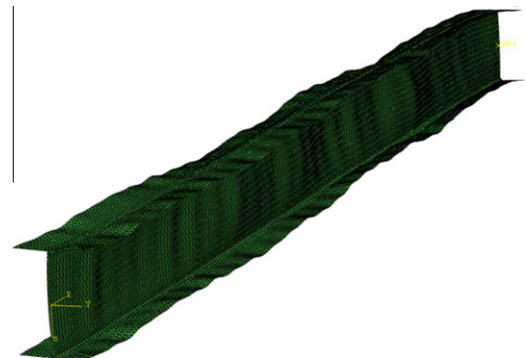

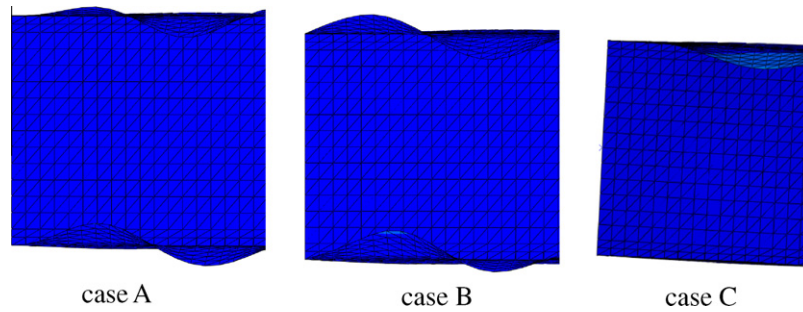**Fig. 5.** Complete imperfect geometry (imperfection modes are scaled by factor $\lambda = 15$).

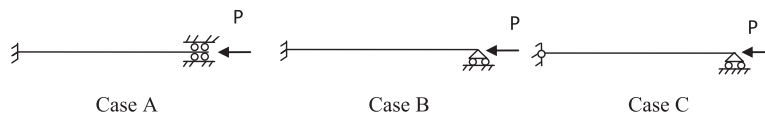**Fig. 6.** Case A, B and C boundary conditions.

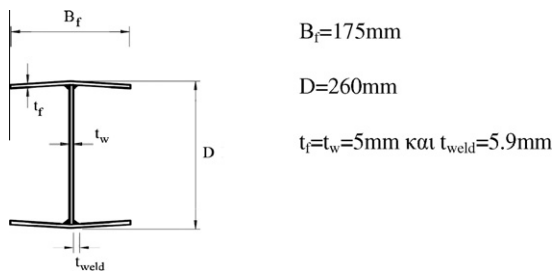**Fig. 7.** Boundary and loading conditions of the three cases examined.

B_f=175mm

D=260mm

t_f=t_w=5mm και t_{weld}=5.9mm

Fig. 8. I-section geometric properties.

4.1.1. FEM discretization

The cross-sectional properties of the beam–column members are depicted in Fig. 8. 3-noded triangular shell finite elements with 6 dof (three translational and three rotational) per node were used for the FEM modeling. The FE discretization of the perfect column configuration is shown in Fig. 9 and consists of 250 elements along the member's longitudinal direction, 12 elements along its width (flanges) and 16 elements along its height (web) with a total of 10,291 nodes and 61,746 dof.

4.1.2. Stochastic analysis

A full material and geometrical nonlinear analysis was performed on each of the 100 samples of imperfect beam–columns generated using Eq. (12) in the context of MC. The Arc Length method was implemented for tracking the unstable branches of the equilibrium path close to bifurcation points. The solution procedure is terminated at an axial deformation of 25 mm. The material is considered to be elasto-plastic with a Von-Mises yield criterion with isotropic hardening equal to the 10% of the elastic Young's modulus $E = 21$ GPa. Fig. 10 presents the histogram of the buckling loads computed for case A boundary conditions, where both ends of the beam–column members are fully fixed (FF). The corresponding buckling load of the perfect beam–column is computed at 1230 kN and the load computed by the eigenvalues analysis, that corresponds to the first global eigenmode is about 960 kN. The mean value of the buckling loads is computed at 975 kN that corresponds to a 20% reduction with respect to the buckling load of the perfect configuration. A relatively small coefficient of variation (Cov) of about 1.1% is observed for this case.

Fig. 11a and b present plots of the deformed shape and the corresponding force–displacement curve computed for a randomly selected imperfect geometry of the member. From this figure it can be observed that the buckling mode triggered by the specific pattern of imperfections is a global minor axis bending. Fig. 12a and b present the same plots with Fig. 11a and b, but for a sample that is located at the extreme left side of the histogram of Fig. 10. From this figure it can be observed that the buckling mode triggered by the specific imperfection pattern is a combined torsional-bending type.

Figs. 13 and 14 present the histograms of the buckling loads computed for cases B and C, respectively. The corresponding buckling loads of the perfect configurations are computed at 1052 kN for both cases. The critical buckling load computed by the
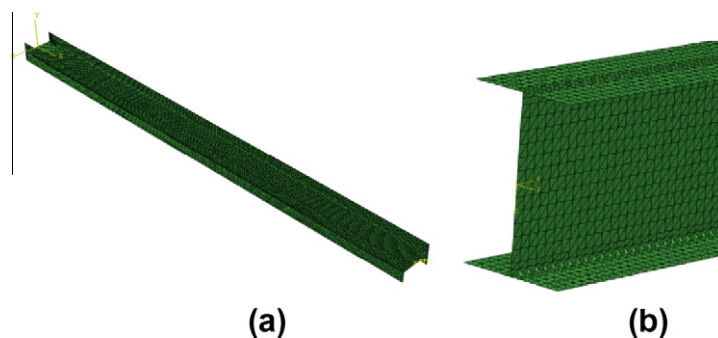

(a)   **(b)**

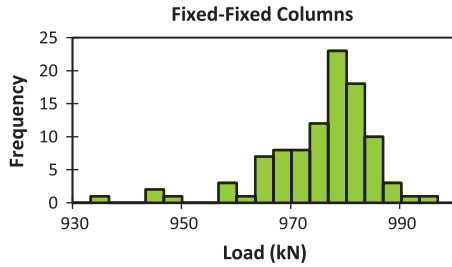**Fig. 9.** (a) Longitudinal and (b) flange and web FE discretization.

Fig. 10. Case A: Histogram of the stochastic critical buckling loads of *FF–FF* members.

and evolves to a global torsional-bending type (point B in Fig. 16c). This behavior is further demonstrated in Fig. 16d where a diagram of the axial force versus the lateral displacement along the *y*-axis direction of the central node of the mid-span cross-section is provided, while Fig. 16e depicts the evolution of the deformations of the mid-span cross-section from the undeformed state to the states at points A, B, C and finally point D, where the analysis is terminated. These results indicate the crucial role that boundary conditions play on the behavior of imperfect I beam–column steel members under axial compression.

4.2. I-section frames

In this section, portal steel frame structures of net 4 m height and span are examined. The frames are constructed with the previously described beam–column members possessing exactly the same imperfection patterns with those described in Section 3. In addition to the aforementioned random imperfections, a random sign parameter (+ or −) is added to the global imperfections ΔY_{glob} and ΔZ_{glob} of Eq. (13) for each beam or column member of the frame. This is done in order to ensure a complete statistical independence between imperfection samples of these members. The beam–column junctions of the frame are assumed to be perfect. The perfect frame FE discretization follows the one described in the previous section for the beam–column members with the addition of beam–columns junctions and their stiffening elements (see Fig. 17). The frames consist of a total of 33,723 nodes, 69,268 elements and 415,608 degrees of freedom.

The nonlinear stochastic analyses of the frames were solved in parallel at five PC clusters with the following technical characteristics: CPU Core i7 X980 @ 3.33 GHz, 12 MB Cache and 6 GB RAM. The total computing time for one stochastic analysis with 100 Monte Carlo simulations was approximately 16 h.
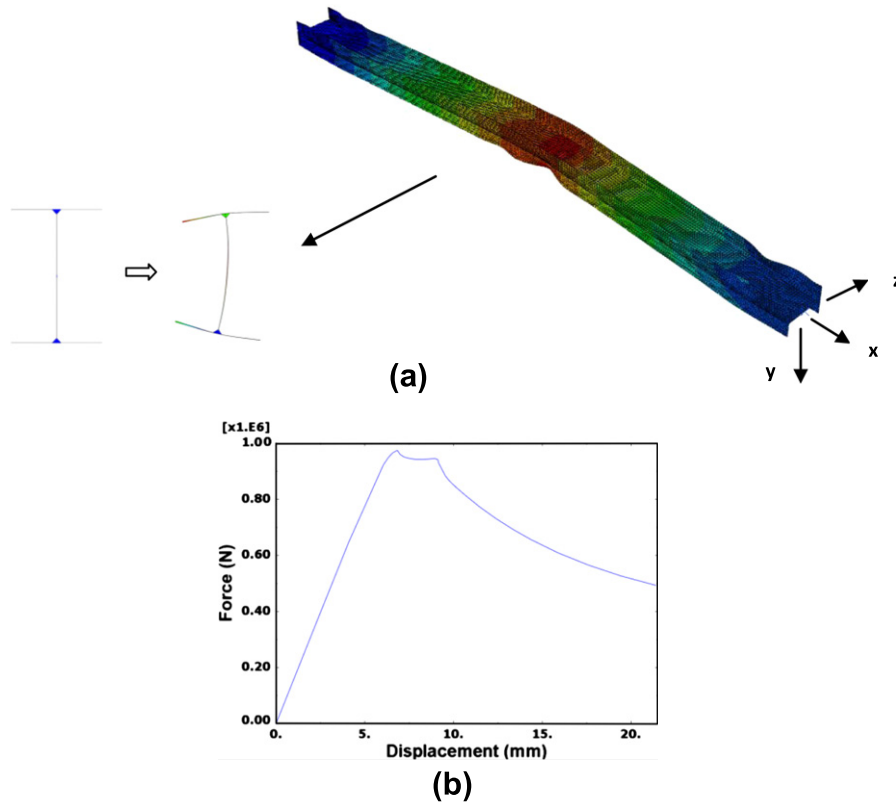
eigenvalue analysis was 962.63 kN for both cases, while the mean values of the buckling loads were computed at 898 kN and 970 kN, respectively, indicating a reduction of almost 15% and 10% with respect to the perfect configurations. Comparing to the critical loads computed by the eigenvalue analysis in case B we have a reduction of the critical buckling load of almost 7%, while in case C the reduction is less than 1%. The Cov was computed at 5.5% and 1.6% for cases B and C, respectively. From these results it can be seen that the case C boundary conditions result in a relatively small mean buckling load with a Cov almost five times larger than the Cov computed for the other examined boundary conditions. Worth mentioning here is that the lowest buckling load for this case is computed at 755 kN which is almost 20% lower from the lowest buckling loads of the two other cases.

Figs. 15 and 16 present plots of the deformed shapes and the force–displacement curves of randomly selected imperfect column for cases B and C, respectively. From these figures it can be observed that the buckling mode triggered by the specific pattern of imperfections in case B is of global bending type (see Fig. 15), while for case C the buckling initiates locally (point A in Fig. 16c)

Fig. 11. Case A: (a) Deformed shape and (b) force–displacement curve along *x*-direction of a random imperfect column under axial compression.
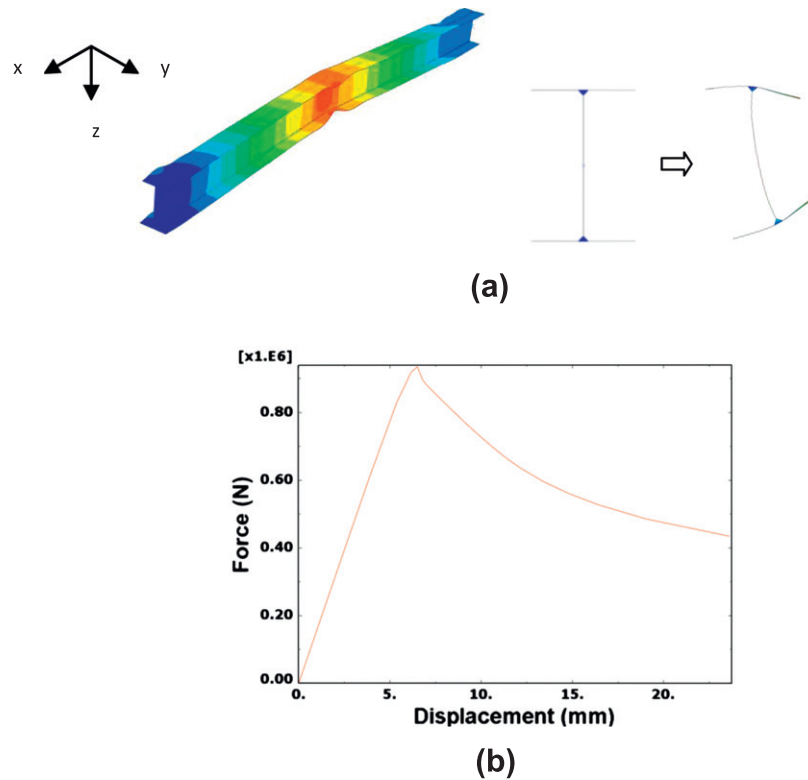
(a)

(b)

Fig. 12. Case A: (a) Deformed shape and (b) force–displacement curve along *x*-direction of a sample located on the extreme left side of Fig. 10.
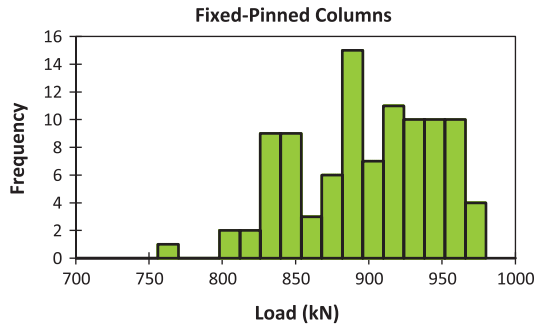

Fig. 13. Case B: Histogram of the stochastic critical buckling loads.
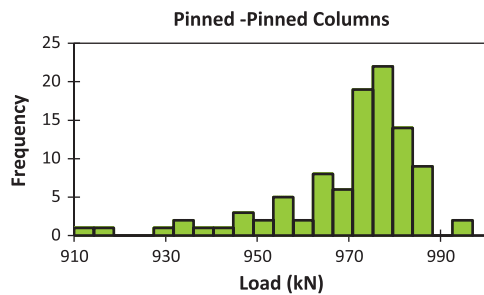

Fig. 14. Case C: Histogram of the stochastic critical buckling loads.

4.2.1. Boundary and loading conditions

As shown in Fig. 18, two different boundary conditions were implemented to the previously described portal frames. In the first case all degrees of freedom of the nodes at both ends are completely restrained, while in the second case the middle nodes of the I-section profile (the nodes on the centroid of the I cross-section) at both ends are considered pinned with respect to major axis rotations, while all translational dof of the remaining nodes are kinematically constrained to their corresponding middle nodes. As far as the junction nodes are concerned (the nodes at the centre of the beam–column junction, see Fig. 17b), these are assumed to be either totally free against all translations and rotations (case A) or restrained against out-of-plane translations (case B), where FF–FF denotes the fully fixed boundary conditions at both ends of the frame and P–P denotes the pinned ones.

Incremental horizontal loads were applied in addition to a permanent vertical self-weight load of the structure. The horizontal load increment is set at $P = 221$ kN uniformly distributed at each node of the left beam–column junction profile (see Fig. 18), which is an area with height 0.255 m and width 0.175 m and is discretized as shown in Fig. 17, while the vertical is 10 kN/m uniformly distributed at each node of the upper flange of the horizontal beam.

4.2.2. Stochastic analysis

A full 3D material and geometrical non-linear analysis has been performed in a sample of 100 imperfect frames for both cases to extract the critical buckling loads of the portal thin-walled steel frames and the results for each case are as follows.

4.2.2.1. Case A: Frame free of out-of-plane restraints. Fig. 19a and b present the histograms of the stochastic critical loads obtained for the frames without out-of-plane restraints for fixed and pinned boundary conditions, respectively. In the case of fixed boundary conditions the mean critical buckling load is computed at 97 kN, with the corresponding buckling load of the perfect configuration being 142 kN – while the buckling load corresponding to the lowest eigenvalue of the perfect structure is 136 kN – indicating a significant strength reduction of about 32%. The Cov for this case is
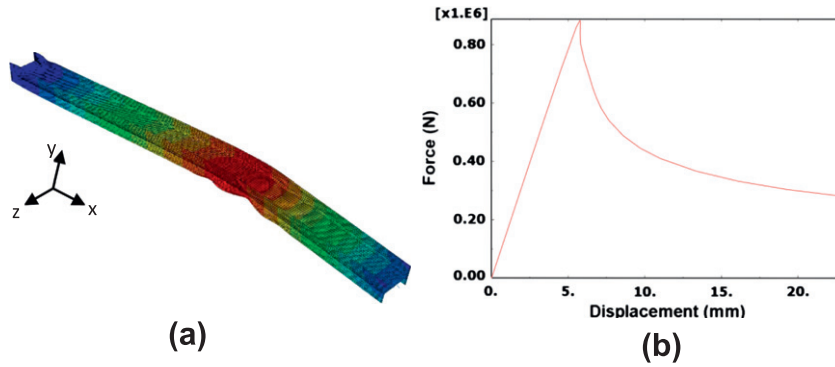
Fig. 15. Case B: (a) Deformed shape and (b) force–displacement along x-direction curve of a random imperfect column under axial compression of a *PF–P* member.

computed at 8%. In the case of pinned boundary conditions, the mean value is computed at 62 kN with the corresponding buckling load of the perfect configuration being 65 kN and the buckling load from the eigenvalue analysis being 75 kN. Thus, a marginal average strength reduction of about 4.6% is observed. The Cov for this case

is computed at 3% which is less than half of the Cov of the fixed case.

Figs. 20 and 21 present the deformed shapes and the force–displacement diagrams of a randomly selected imperfect fixed frame and its corresponding perfect frame, respectively. As can
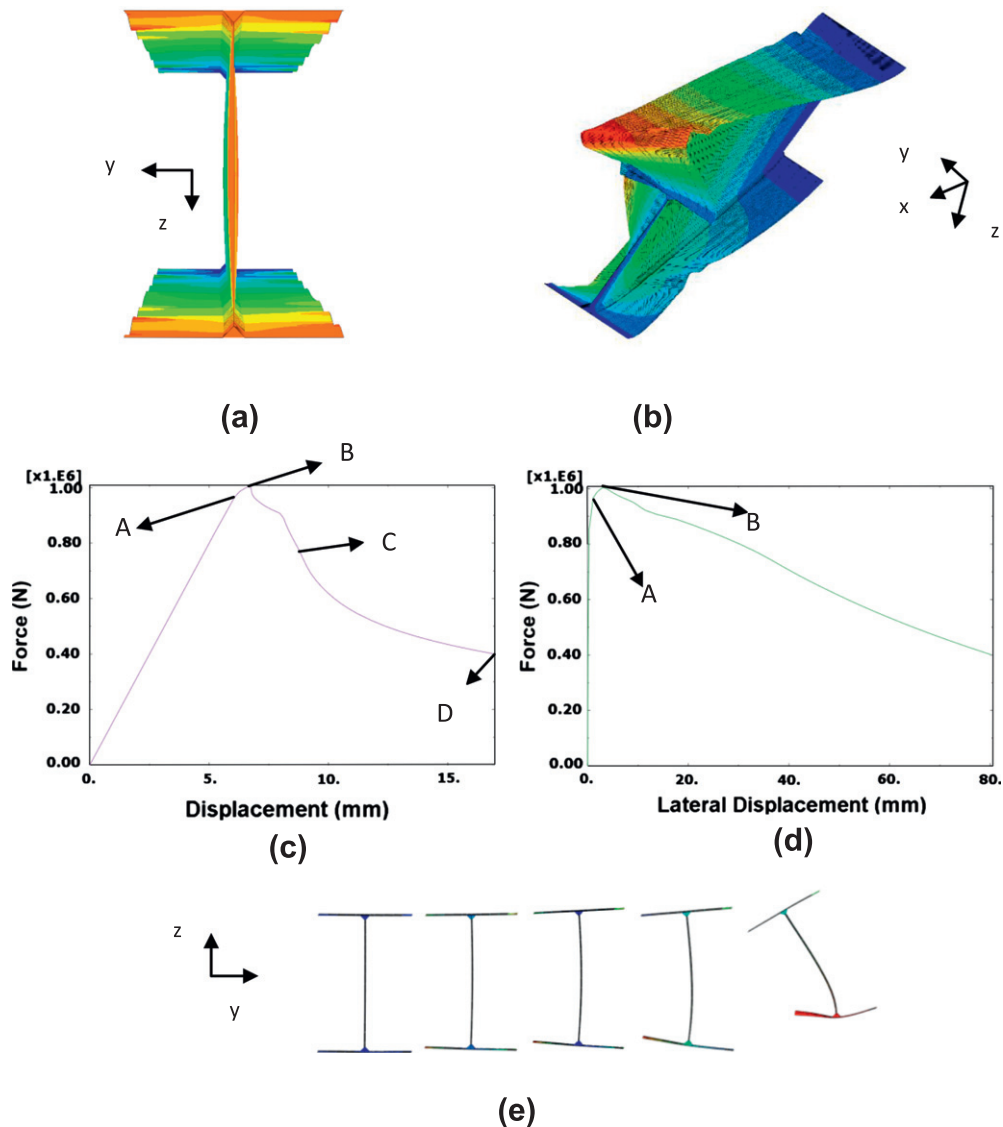
Fig. 16. Case C: (a) Deformed shape at point A, (b) deformed shape after point B, (c) force–displacement curve along x-axis, (d) axial force–lateral displacement of the mid-span along the y-axis direction, and (e) evolution of deformations of mid-span cross-section at points 0, A, B, C and D.
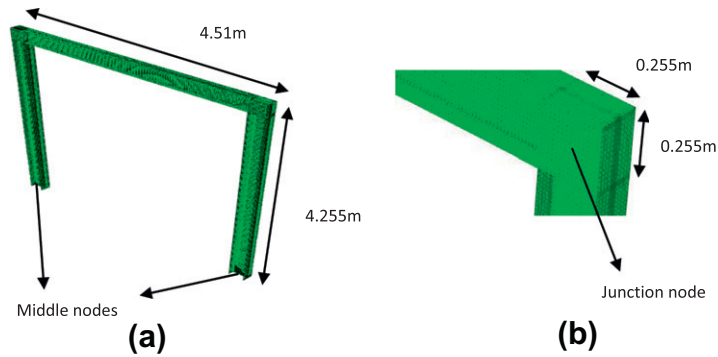
Fig. 17. (a) Portal frame and (b) detail of beam–column junction discretization.

be seen in these figures, the buckling mode triggered by the specific imperfection pattern is a bifurcation buckling of torsional type with out-of-plane bending of the columns. Worth noting is that
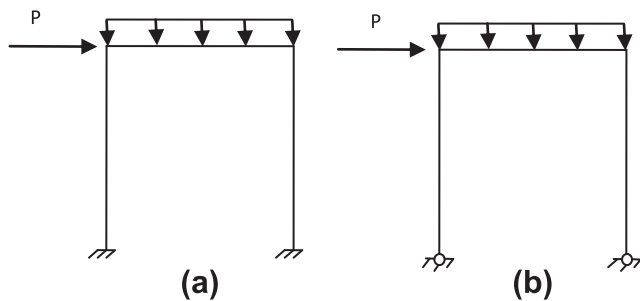

Fig. 18. Loading and boundary condition case (a) *FF–FF* and (b) *P–P*.

some samples at the extreme right part of the histogram reach the buckling resistance of the perfect configuration that corresponds to a predominant local elasto-plastic buckling scenario of the columns. In these cases the corresponding buckling modes are the same with the ones of the perfect structure, i.e. minor axis bending buckling but without a global torsional behavior (Fig. 21).

Figs. 22 and 23 present the deformed shapes and the corresponding force–displacement curves of a randomly selected imperfect pinned frame and its corresponding perfect frame, respectively. As can be seen in these figures, the buckling mode triggered by the specific imperfection pattern is an out-of-plane bending type but without torsion. In addition, local bucking is observed at the initiation of the structural non-linear response. This buckling mode is almost the same with the corresponding buckling mode of the perfect configuration (Fig. 23). This also explains the fact that the mean buckling load in this case is marginally lower
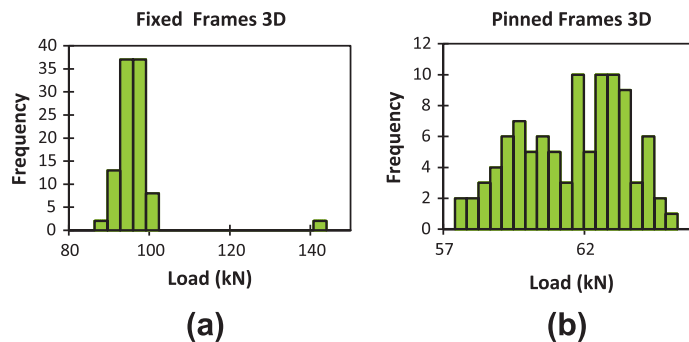

Fig. 19. Histogram of the critical buckling loads of (a) imperfect fixed and (b) imperfect pinned frames.
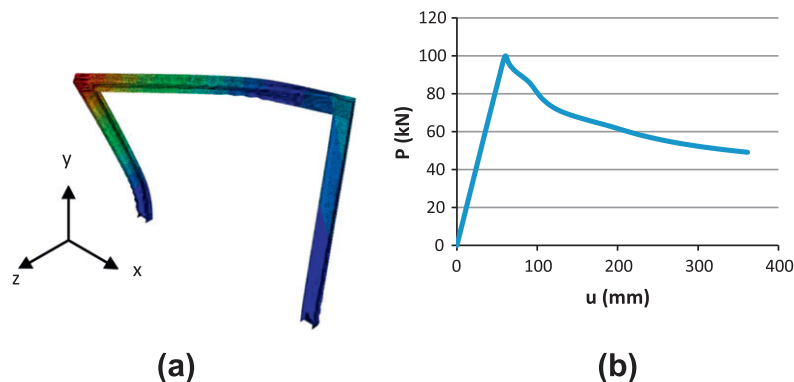

Fig. 20. (a) Deformed shape and (b) force–displacement curve along *x*-axis direction of an imperfect fixed frame.

than the corresponding buckling load of the perfect structure followed by a very small value of the Cov.

4.2.2.2. Case B: Frame with out-of-plane restraints. Fig. 24a and b show the histograms computed for the fixed and pinned frames of case B, respectively. Fixed frames have a mean critical buckling load around 144 kN with a Cov up to 1.5%. This corresponds to an average strength reduction with respect to the perfect frame of only 1.5%, while the critical buckling load corresponding to the lowest eigenvalue of the perfect structure is 137 kN. In the case of pinned frames the computed mean value of the buckling loads is 64 kN with a Cov of about 2.11% and an average strength reduction with respect to the perfect configuration again 1.5%, while the critical buckling load corresponding to the lowest eigenvalue of the
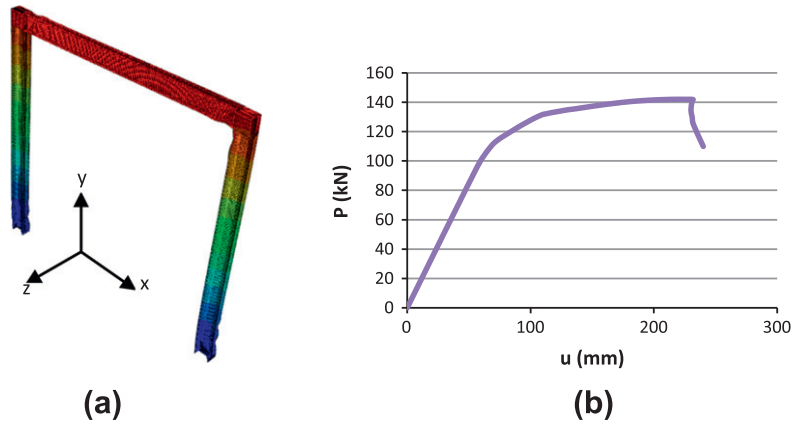

Fig. 21. (a) Deformed shape and (b) force–displacement curve along x-axis direction of the perfect fixed frame.
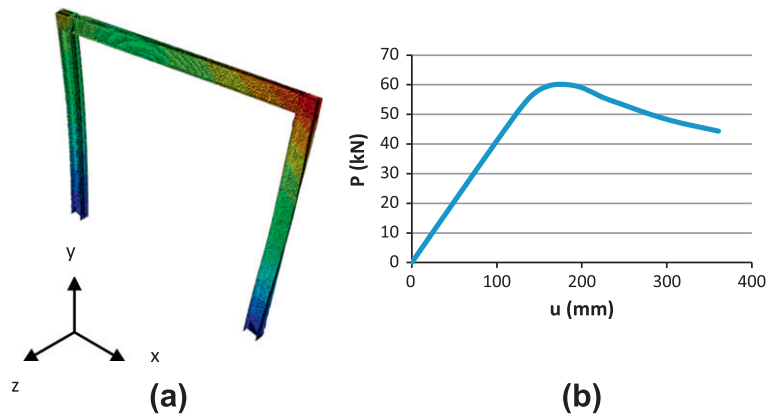

Fig. 22. (a) Deformed shape and (b) force–displacement along x-axis direction curve of pinned frame.
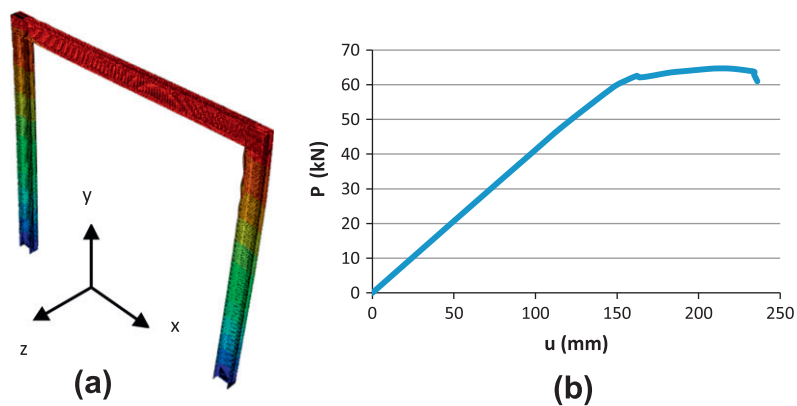

Fig. 23. (a) Deformed shape and (b) force–displacement curve along x-axis direction of the perfect pinned frame.
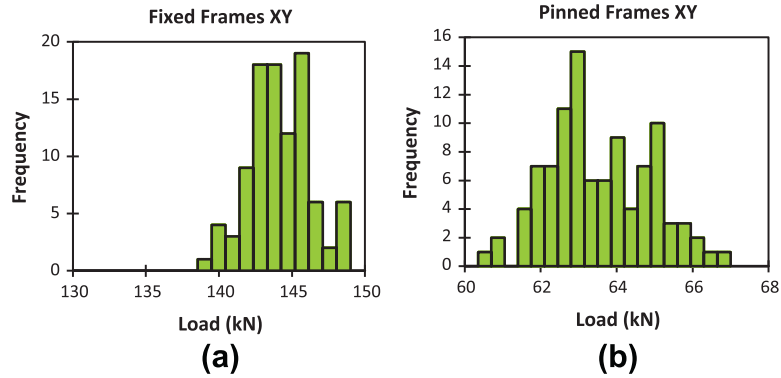
Fig. 24. Histogram of the stochastic critical buckling loads of (a) imperfect fixed and (b) imperfect pinned frames.
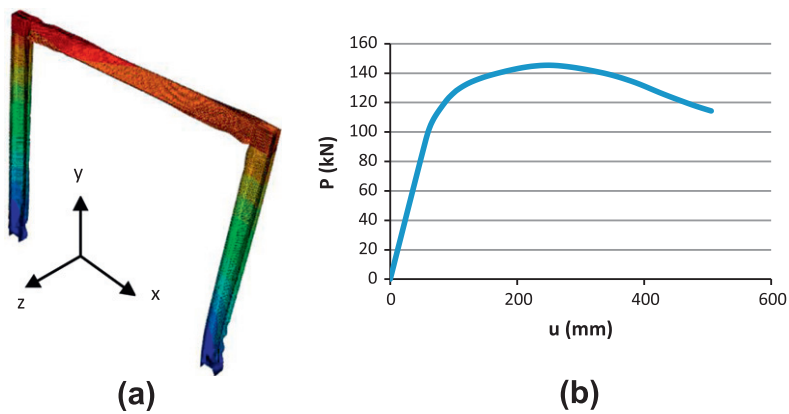

Fig. 25. (a) Deformed shape and (b) P–u curve along x-axis direction of an imperfect fixed frame.
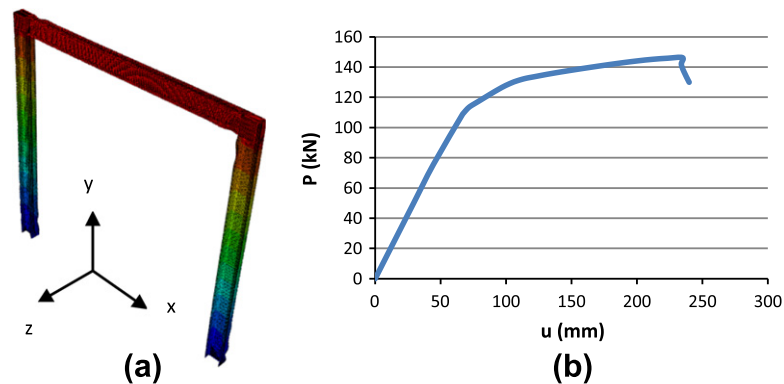

Fig. 26. (a) Deformed shape and (b) P–u curve along x-axis direction of the perfect fixed frame.

perfect structure is 75 kN. Thus, in both cases the variability of buckling loads is relatively small and close to the value of the perfect configuration.

Figs. 25 and 26 present the deformed shapes and the corresponding force–displacement curves of a randomly selected imperfect fixed frame and its corresponding perfect configuration. As can be seen in these figures, in both imperfect and perfect frames the behavior is a local elasto-plastic buckling one with an out-of-plane bending mode without torsion.

Figs. 27 and 28 present the same results with Figs. 25 and 26 but for the pinned frame. Again from these figures it can be

seen that the response of imperfect and perfect frames is similar, undergoing a local elasto-plastic buckling behavior with out-of-plane bending buckling of the columns with no torsion. Thus for both boundary conditions applied in case B, the imperfections seem to play a minor role in their buckling behavior.

It should be mentioned here that, as in the case of imperfect beam–column members in [20], the effect of material and thickness imperfections is expected to have a minor influence the buckling behavior in this type of structures. This influence however, remains to be quantified in future research.
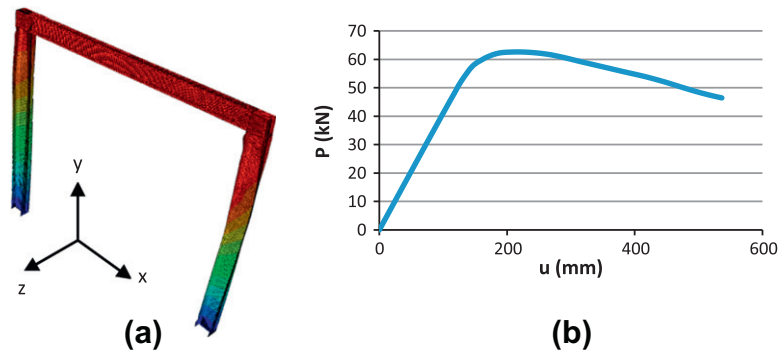
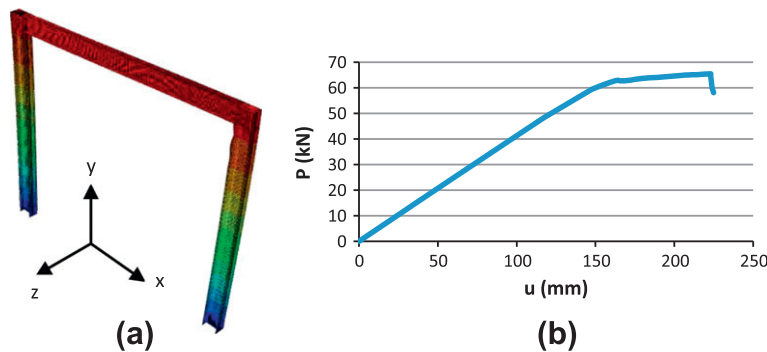**Fig. 27.** Case B: (a) Deformed shape and (b) *P–u* curve along *x*-axis direction of an imperfect *P–P* frame.

Fig. 28. Case B: (a) Deformed shape and (b) *P–u* curve along *x*-axis direction of the perfect *P–P* frame.

5. Conclusions

The present paper implements a general SFEM approach for treating random initial geometric imperfections of I section steel beam–column members and portal frame structures. The methodology is based on the method of separation recently proposed for extracting accurately the evolutionary characteristics of the power spectrum of measured initial imperfections. Using this approach it is made possible to quantify buckling load variability as well as the strength reduction that occurs in imperfect I section steel beam–column members and portal frame structures and address their sensitivity to various types of boundary conditions.

Acknowledgment

References

[1] Ramm E, Wall W. Shell structures: a sensitive interrelation between physics and numerics. Int J Numer Meth Eng 2004;60:381–427.
[2] Trahair NS, Bradford MA, Nethercot DA, Gardner L. The behavior and design of steel structures to EC3. New York: Taylor and Francis; 2008.
[3] Rasmussen KJR, Hancock GJ. Buckling analysis of thin-walled structures: numerical developments and applications. Prog Struct Eng Mater 2000;2(3):359–68.
[4] Palassopoulos GV. Buckling analysis and design of imperfection sensitive structures. In: Haldar A, Guran BM, Ayyub, editors. Uncertainty modeling in finite element, fatigue and stability of systems, vol. 9. Series on stability, vibration and control of system series B. Singapore: World Scientific Publishing Company; 1977. p. 311–56.
[5] Koiter WT. The effect of axisymmetric imperfections on the buckling of cylindrical shells under axial compression. Proc Koninkl Nederl Akademie van Wetenschappen 1963;66(B):265–79.
[6] Arbocz J, Babcock Jr CD. The effect of general imperfections on the buckling of cylindrical shells. J Appl Mech 1969;36(1):28–38.
[7] Arbocz J, Starnes Jr JH. Future directions and challenges in shell stability analysis. Thin Walled Struct 2002;40:729–54.
[8] Arbocz J, Hol JMAM. Koiter's stability theory in a computer aided engineering (CAE) environment. Int J Solids Struct 1991;26(9–10):945–73.
[9] Elishakoff I. Uncertain buckling: its past, present and future. Int J Solids Struct 2000;37:6869–89.
[10] Schafer BW, Grigoriu M, Pekoz T. A probabilistic examination of the ultimate strength of cold-formed steel elements. Thin-Walled Struct 1998;31:271–88.
[11] Basundhar A, Missoum S. A sampling-based approach for probabilistic design with random fields. Comput Methods Appl Mech Eng 2009;191(47–48):3647–55.
[12] Chen N-Z, Guedes Soares C. Spectral stochastic finite element analysis of laminated composite plates. Comput Methods Appl Mech Eng 2008;197:4830–9.
[13] Craig KJ, Roux WJ. On the investigation of shell buckling due to random geometrical imperfections implemented using Karhunen-Loeve expansions. Int J Numer Methods Eng 2008;73:1715–26.
[14] Kolanek K, Jendo S. Random field models of geometrically imperfect structures with "clamped" boundary conditions. Prob Eng Mech 2008;23(2):219–26.
[15] Papadopoulos V, Papadrakakis M. Finite element analysis of cylindrical panels with random initial imperfections. J Eng Mech 2004;130:867–76.
[16] Papadopoulos V, Papadrakakis M. The effect of material and thickness variability on the buckling load of shells with random initial imperfections. Comput Methods Appl Mech Eng 2005;194:1405–26.
[17] Papadopoulos V, Iglesis P. The effect of non-uniformly of axial loading ont the buckling behavior of shells with random imperfections. Int J Solids Struct 2007;44:6299–317.
[18] Papadopoulos V, Charmpis DC, Papadrakakis M. A computationally efficient method for the buckling analysis of shells with stochastic imperfections. Comput Mech 2008;43:687–700.
[19] Papadopoulos V, Stefanou G, Papadrakakis M. Buckling analysis of imperfect shells with stochastic non-Gaussian material and thickness properties. In J Solids Struct 2009;46:2800–8.
[20] Schillinger D, Papadopoulos V, Bischoff M, Papadrakakis M. Buckling analysis of imperfect I-section beam-columns with stochastic shell finite elements. Comput Mech 2010.
[21] Schillinger D, Papadopoulos V. Accurate estimation of evolutionary power spectra for strongly narrow-band random fields. Comput Methods Appl Mech Eng 2009.
[22] Broggi M, Schuëller GI. Efficient modeling of imperfections for buckling analysis of composite cylindrical shells. Eng Struct 2011;33(5):1796–806.
[23] Papoulis A, Pillai SU. Probability, random variables and stochastic processes. New York: McGraw-Hill; 2002.
[24] Shinozuka M, Deodatis G. Simulation of stochastic processes by spectral representation. Appl Mech Rev (ASME) 1991;44:191–203.

[25] Shinozuka M, Deodatis G. Simulation of multi-dimensional Gaussian stochastic fields by spectral representation. Appl Mech Rev (ASME) 1996;49:29–53.

[26] Stefanou G, Papadrakakis M. Assessment of spectral representation and Karhunen-Loeve expansion methods for the simulation of Gaussian stochastic fields. Comput Methods Appl Mech Eng 2007;196:2465–77.

[27] Stefanou G. Stochastic finite element method: past, present and future. Comput Methods Appl Mech Eng 2009;198:1031–51.

[28] Sudret B, Der Kiureghian A. Stochastic finite element methods and reliability: a state-of-the-art report. Rep. No. UCB/SEMM-2000/08. University of California at Berkeley, USA; 2000.

[29] Newland DE. Wavelet analysis of vibration, part I: Theory. J Vib Acoust 1994;116:409–16.

[30] Newland DE. Wavelet analysis of vibration, part II: Wavelet maps. J Vib Acoust 1994;116:417–25.

[31] Mallat S. A wavelet tour of signal processing. New York: Academic Press; 1999.

[32] Spanos PD, Tezcan J, Tratskas P. Stochastic processes evolutionary spectrum estimation via harmonic wavelets. Comput Methods Appl Mech Eng 2005;194:1367–83.

[33] Cohen L. Time-frequency analysis. New Jersey: Prentice Hall; 1995.

[34] Rubinstein RY, Kroese DP. Simulation and the Monte Carlo Method. John Willey and Sons; 2008.

[35] Sobol I. A primer for the Monte Carlo Method. New York: CRC Press; 1994.

[36] Fishman G. Monte Carlo: concepts, algorithms and applications. New York: Springer; 2001.

[37] Hasham AS, Rasmussen KJR. Member capacity of thin-walled I-sections in combined compression and major axis bending. Report research R746. School of Civil Engineering, University of Sydney; 1997.